Photometrically-corrected global infrared mosaics of Enceladus: New implications for its spectral diversity and geological activity

Rozenn Robidel[a,*], Stéphane Le Mouélic[a], Gabriel Tobie[a], Marion Massé[a], Benoît Seignovert[b], Christophe Sotin[b], Sébastien Rodriguez[c]

[a] *Laboratoire de Planétologie et Géodynamique, UMR 6112, CNRS, Université de Nantes, Nantes, France*
[b] *Jet Propulsion Laboratory, California Institute of Technology, Pasadena CA, USA*
[c] *Université de Paris, Institut de Physique du Globe de Paris, CNRS, Paris, France*

arXiv:2006.00146v2 [astro-ph.EP] 10 Jun 2020

Abstract

Between 2004 and 2017, spectral observations have been gathered by the Visual and Infrared Mapping Spectrometer (VIMS) on-board Cassini (Brown et al., 2004) during 23 Enceladus close encounters, in addition to more distant surveys. The objective of the present study is to produce a global hyperspectral mosaic of the complete VIMS data set of Enceladus in order to highlight spectral variations among the different geological units. This requires the selection of the best observations in terms of spatial resolution and illumination conditions. We have carried out a detailed investigation of the photometric behavior at several key wavelengths (1.35,1.5, 1.65, 1.8, 2.0, 2.25, 2.55 and 3.6 µm), characteristics of the infrared spectra of water ice. We propose a new photometric function, based on the model of Shkuratov et al. (2011) When combined, corrected mosaics at different wavelengths reveal heterogeneous areas, in particular in the terrains surrounding the Tiger Stripes on the South Pole and in the northern hemisphere around 30°N, 90°W. Those areas appear mainly correlated to tectonized units, indicating an endogenous origin, potentially driven by seafloor hotspots.

Keywords: Enceladus, Cassini, VIMS, Spectrophotometry, Image processing
*doi:*10.1016/j.icarus.2020.113848

1. Introduction

During its 13 years orbital tour around Saturn, the Cassini spacecraft has acquired a significant amount of observations of Saturn's icy satellites, including Enceladus, an active icy moon only 500 km in diameter. Enceladus has an unusually high reflectance due to a surface composed mostly of pure water ice (Buratti and Veverka, 1984; Cruikshank et al., 2005; Brown et al., 2006; Dalton et al., 2010). Early observations from the Voyager era (Smith et al., 1982; Squyres et al., 1983) suggest that Enceladus experienced recent resurfacing and volcanic activity. In 2005, after a first hint from the Cassini magnetometer (Dougherty et al., 2006), various instruments of the Cassini spacecraft identified the presence of active jets of water vapor and ice grains emanating from four main warm faults at the South Pole, named Tiger Stripes (Hansen et al., 2006; Porco et al., 2006; Spencer et al., 2006; Waite et al., 2006). This discovery confirms that Enceladus is volcanically active and is the main source of Saturn's E ring, the farthest ring from the planet (Spahn et al., 2006).

The Visual and Infrared Mapping Spectrometer (VIMS) onboard the Cassini spacecraft (Brown et al., 2004) provided compositional evidence of activity at Enceladus' South Pole. The analysis of VIMS data provides not only information about the composition of the surface but also the physical state (grain size and degree of crystallinity) of the surface materials and the temperature of the surface (Jaumann et al., 2008; Taffin et al., 2012; Filacchione et al., 2016). Crystalline water ice with grain size 100 µm as well as CO_2 and light organics were found along the Tiger Stripes (Brown et al., 2006; Jaumann et al., 2008; Newman et al., 2008; Scipioni et al., 2017). Combe et al. (2019) provided the first complete map of CO_2 of Enceladus' surface. They confirmed that CO_2 is mostly located in the south polar terrain, as CO_2 ice and in complexed form, possibly CO_2 clathrate hydrate (Oancea et al., 2012). They also noticed possible detection of CO_2 in the northern hemisphere around 60°N, 270°W and around the North Pole between 70°N and 80°N (absorption band depth at 4.24 µm) as well as around 30–40°N, 100°W (absorption band depth at 2.7 µm). These findings need further investigation as only one of the two absorption bands characteristics of CO_2 was observed. Scipioni et al. (2017) investigated the variation of the main water ice absorption bands and of the sub-micron ice grains spectral features, enhancing the Tiger Stripes. Furthermore, they pointed out an abnormally bright behavior around 30°N, 90°W which does not seem, a priori, to be related to any obvious morphological structure. Interestingly, Ries and Janssen (2015) detected a microwave scattering anomaly covering the same area.

*Corresponding author: rozenn.robidel@gmail.com

In Combe et al. (2019) and (Scipioni et al., 2017), no photometric correction was applied during the processing of the spectra. In the present study, we investigate this aspect, to refine the spectral analysis and compositional mapping. Indeed, the brightness of an object depends on the intrinsic properties of the surface materials (composition, grain size, roughness, porosity etc.) and the surface shape but also on the geometry of illumination and observation. To construct surface reflectance maps from VIMS hyperspectral cubes taken at varying geometries, photometric analyses are to be achieved. It is also needed for comparing surface spectral reflectance from one region to another observed under different geometries and interpreting the composition based on laboratory measurements, taken at geometries different from the planetary observations. To correct the surface reflectance from the geometry effects, several photometric models have been developed (*e.g.,* Hapke, 1963, 1981, 2012; Minnaert, 1941; Shkuratov et al., 2011). Here we adapt the approach of Shkuratov et al. (2011) which has been applied on other Saturnian moons by Filacchione et al. (2018a,b). In this work, we carry a detailed photometric analysis in order to derive an optimal photometric function of Enceladus' surface at different wavelengths. In sections 2 and 3, we present the parametrization of the photometric function and the construction of the global mosaics. This parametrization takes into account various viewing and illumination conditions which allows us to produce global mosaics of the complete dataset of Enceladus acquired by Cassini VIMS during the entire mission. We then discuss in section 4 the spectral diversity and the implications of these new compositional mappings for the geological activity of Enceladus.

2. VIMS dataset and methods for computing global maps

2.1. Observations and data selection

VIMS acquired hyperspectral cubes composed of images taken at 352 spectral channels ranging from 0.35 to 5.12 µm (Brown et al., 2004). The instrument consisted of two imaging spectrometers. The first one operated in the visible range (0.35–1.04 µm) over 96 spectral channels whereas the second one covered a wavelength range from 0.88 to 5.12 µm over 256 spectral channels. Images were up to 64×64 pixels, the size depending on the operation mode (image, line, point or occultation) and observation conditions (fast flyby, particular geometry, simultaneous observation with the Imaging Science Subsystem - ISS).

All the data cubes have been calibrated in radiance factor (Hapke, 1981):

$$r_F = \pi r \tag{1}$$

Where the r is the bidirectional reflectance of the surface. It is defined as follows:

$$r(i, e, \alpha, \lambda) = \frac{I(i, e, \alpha, \lambda)}{J(\lambda)} \tag{2}$$

Where I is the radiance in W.m^{-2}.µm^{-1}.sr^{-1}, J is the normal solar irradiance in W.m^{-2}.µm^{-1}, λ is the wavelength, i is the local angle of incidence, e is the local angle of emergence and α is the phase angle. The radiance factor is also known as I/F (with $F = J/\pi$). We use the term *reflectance* for the radiance factor in the remainder of this paper.

To convert digital count number of each pixel into physical radiance, the calibration pipeline (background subtraction, flat fielding, conversion into specific energy, division by the solar spectrum and despiking) used is RC19 (Clark et al., 2018). Due to the spectral drift in wavelength of the spectral channel, data are realigned on a common spectral base with a spline interpolation, using the shifts evaluated by Clark et al. (2018). Navigation information, such as geographic position (latitude and longitude position at the pixel's center and at the four corners of the pixel), corresponding illumination and viewing conditions (incidence, emergence and solar phase angles at each pixel's center) and spatial resolution, were retrieved using reconstructed SPICE kernels (Acton, 1996). The pixel location is calculated as the intersection between Enceladus mean radius (252.1 km) and the VIMS pixel boresight (Nicholson et al., 2019). Our projected VIMS cubes are geometrically consistent with the latest ISS global map (Bland et al., 2018) as it can been on a few examples on Fig. 11.

During the 13 years of the Cassini mission, 147 flybys of Enceladus were performed, 23 of which were targeted. We reported a total of 14,742 hyperspectral cubes acquired throughout the mission, 2486 of which were out of scope or pointing at the night side, thus not relevant for the surface mapping.

The imaging data acquired on planetary surfaces strongly depends on the angles at which they are observed. These conditions vary according to the orbit, the seasons and the sun's illumination. When the acquisition geometry is too extreme, *e.g.,* very high angles or grazing observation conditions, data are difficult to reconcile with each other into homogeneous mosaics. Unfavorable observation geometry is generally not suitable to produce global maps. To avoid those unfavorable observation geometries, we have applied thresholds on the incidence and emergence angles. We considered only observations acquired on the dayside of Enceladus. We have performed several tests and reached a compromise between spatial coverage and mosaic quality by limiting the local angles of incidence and emergence to 80°. In addition, we consider only hyperspectral cubes with a spatial resolution better than 20 km/pixel in order to have the most resolved dataset. Finally, cubes which are partially or totally saturated are not considered. To discard unusable cubes, we use the vims website vims.univ-nantes.fr which provides a user-friendly access to multispectral summary images, produced from Planetary Data System archive and covering the entire mission.

When restrained to these conditions, the number of useful VIMS cubes is reduced to 355, acquired during the most

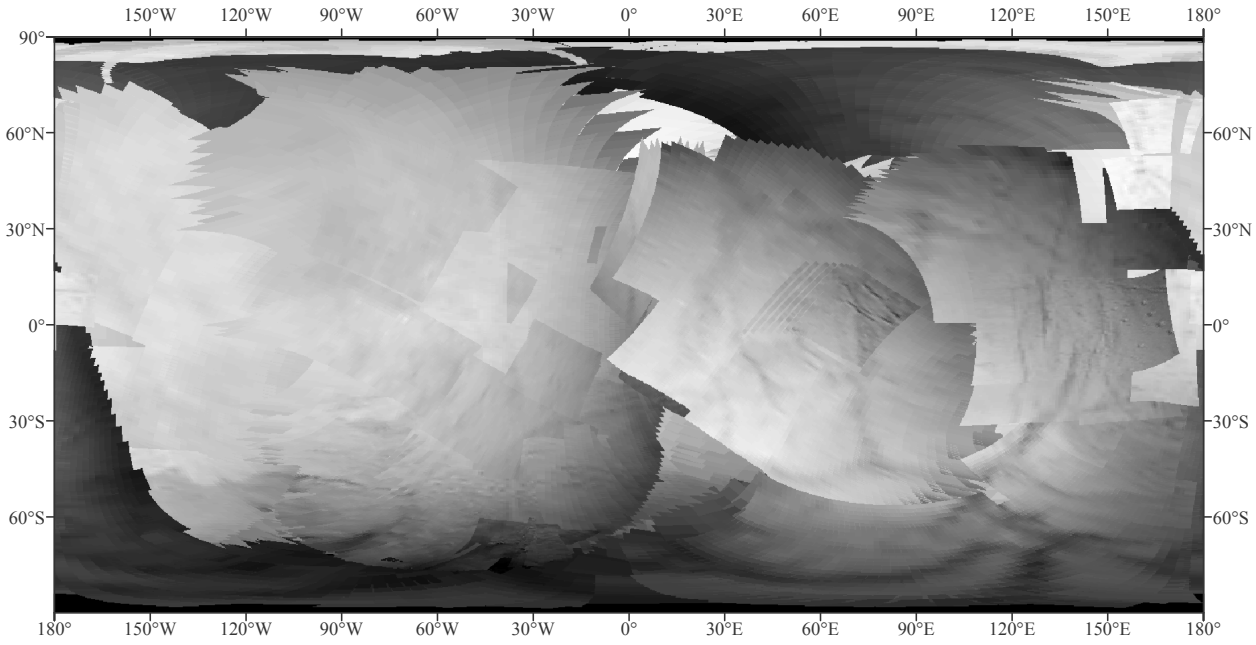


Fig. 1. *Global mosaic in equirectangular projection at 1.8 µm, containing all the 355 VIMS cubes responding to thresholds mentioned in section 2.1, before the photometric correction.*

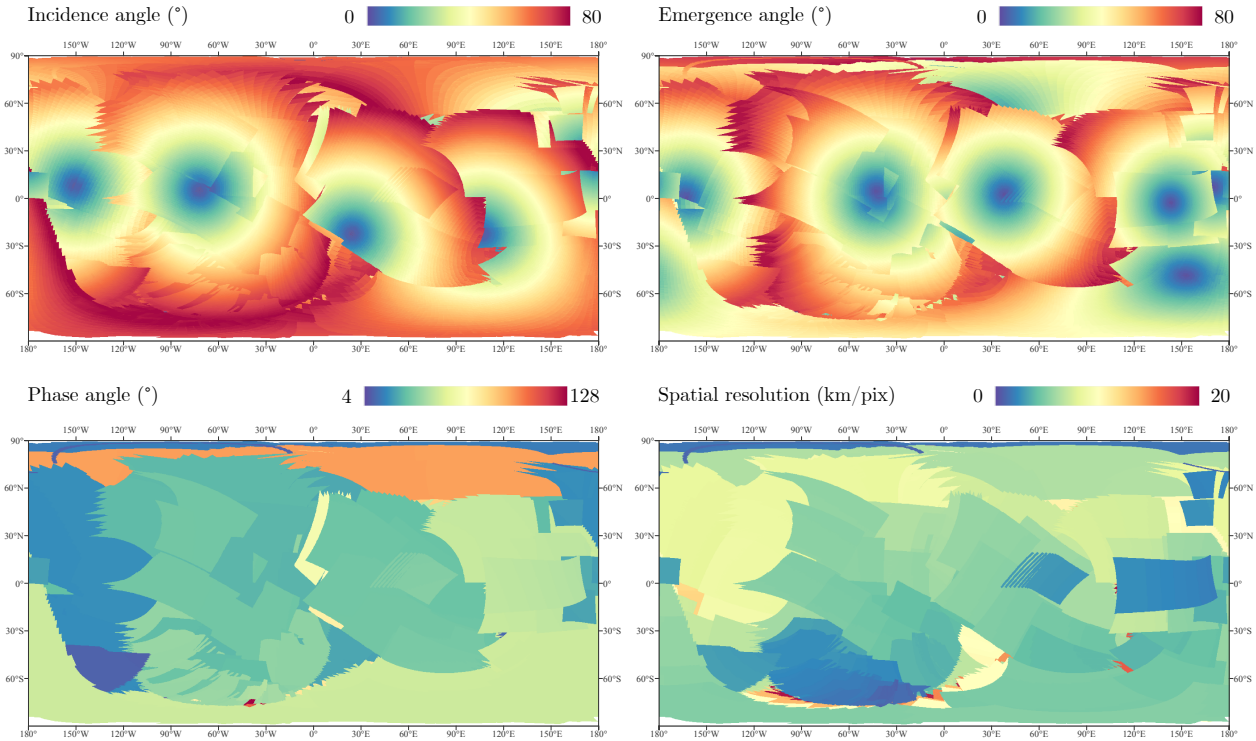


Fig. 2. *Global mosaics of incidence, emergence, phase angles and the pixel spatial resolution.*

favorable flybys. They come from revolutions 3, 4, 11, 88, 91, 120, 121, 131, 136, 141, 142, 153, 158, 223, 228, 230 and 250.

2.2. Merging data into global maps

Global maps are generated by sorting the 355 cubes in decreasing order of spatial resolution, which puts the most resolved images on top of the map. This method has been successfully applied to Titan (Le Mouélic et al., 2019). The resulting global mosaic, including 355 selected cubes (Fig. 1), shows high contrasted seams and illumination residuals due to the lack of an appropriate photometric correction.

Although we did not apply any threshold on the solar phase angle, the imposed limitations on the incidence and emergence angles have resulted in phase angle ranging

from 4° to 128° (Fig. 2). As shown in Fig. 2, illustrating the relevant observation parameters, the observation conditions can locally strongly vary from one flyby to another. This effect can be partially corrected by applying an appropriate photometric function. We will focus on the derivation of this function in the next step.

3. Derivation of a parametrized photometric correction function

3.1. Model description

The application of a photometric correction is an essential step in obtaining a map expressing the surface variability in terms of composition and physical state. In fact, the observed brightness of the surface depends on both illumination and viewing geometry.

To model the photometric behavior, different models have been proposed (Minnaert, 1941; Buratti and Veverka, 1985; Shkuratov et al., 2011), one of the most commonly used being the model of Hapke (1963, 1981, 2012). Previous studies of Enceladus' photometry only dealt with Voyager and Earth-based data, hence with low resolution (Buratti, 1984; Buratti and Veverka, 1984; Verbiscer and Veverka, 1994). Buratti (1984), tested an empirical expression and Minnaert's model (eqs. (1) and (2) in Buratti, 1984), while Verbiscer and Veverka (1994) tested Hapke's model.

In this study, we have decided to adopt the method given by Shkuratov et al. (2011). The photometric correction is therefore separated in two parts; the disk function $D(i, e, \alpha)$ and the phase function $A_{\rm eq}(\alpha, \lambda)$ that includes the albedo:

$$I/F(i, e, \alpha, \lambda) = D(i, e, \alpha) \cdot A_{\rm eq}(\alpha, \lambda) \quad (3)$$

Similar approach has been previously applied on the Earth's Moon (Shkuratov et al., 1999, 2011; Kreslavsky et al., 2000), Mercury (Domingue et al., 2016), Vesta (Schröder et al., 2013; Combe et al., 2015), Ceres (Schröder et al., 2017), Tethys and Dione (Filacchione et al., 2018a,b).

We have evaluated different disk functions (Minnaert, 1941; Akimov, 1976, 1988). We also have tested the case of parametrized Akimov (eq. (19) in Shkuratov et al., 2011). The models' equations and results are provided in supplementary material (Fig. A.1, Fig. A.2 and Table A.2). The standard deviation errors of Akimov model and parametrized Akimov model, associated with a linear phase, are fairly close. However, the Akimov model provides the best result in terms of mosaic quality, therefore, in the remainder of this paper, we use Akimov disk function, defined as follows:

$$D(i, e, \alpha) = \cos\left(\frac{\alpha}{2}\right) \cdot \cos\left[\frac{\pi}{\pi - \alpha}\left(\gamma - \frac{\alpha}{2}\right)\right] \cdot \frac{(\cos\beta)^{\frac{\alpha}{\pi-\alpha}}}{\cos\gamma} \quad (4)$$

The photometric latitude β and longitude γ are related to the local angles of incidence and emergence as follows:

$$\cos i = \cos\beta \cdot \cos(\alpha - \gamma) \quad (5)$$
$$\cos e = \cos\beta \cdot \cos\gamma \quad (6)$$

The phase function, or equigonal albedo, $A_{\rm eq}(\alpha, \lambda)$, represents the phase dependence of brightness. It can be expressed as follows:

$$A_{\rm eq}(\alpha, \lambda) = A\left(\alpha_0, \lambda\right) \cdot f(\alpha, \lambda) \quad (7)$$

Where $f(\alpha, \lambda)$ is the phase function normalized to unity at $\alpha = \alpha_0 = 0°$ and $A\left(\alpha_0, \lambda\right)$ is the equigonal albedo value at $\alpha = \alpha_0 = 0°$ (Shkuratov et al., 2011). The phase function is derived by applying a fit of arbitrary functional form to the observation data corrected for the disk function. We have tested both exponential fit and polynomial fits of various degrees and noticed that a linear fit is satisfactory. Hence, the following linear fit is used:

$$A_{\rm eq}(\alpha, \lambda) = a(\lambda) + b(\lambda) \cdot \alpha \quad (8)$$

We can notice that the parameter a corresponds to the equigonal albedo value at $\alpha = 0°$.

A few examples showing that the equigonal albedo varies linearly with the phase angle are given in the next section (Fig. 4).

3.2. Phase curve fitting at selected wavelengths

In the range 0.88–5.12 µm, water ice exhibits strong features (1.04, 1.25, 1.5, 1.65, 2.0 and 3.1 µm). The existence, position, shape, intensity and width of absorption bands are characteristics of the structure of the ice as well as its temperature and grain size (Fink and Larson, 1975; Clark and Lucey, 1984; Brown et al., 2006; Newman et al., 2008; Clark et al., 2013; Scipioni et al., 2017). The deeper the absorption, the higher the abundance and the grain size. The reflectance peak at 3.6 µm is also an indicator of the grain size, the greater the intensity of the peak, the smaller the grain size will be (Hansen and McCord, 2004; Filacchione et al., 2012). The 1.65 µm absorption band and the 3.1 µm Fresnel reflection peak are the two most obvious indicators of crystallinity, both of which are much prominent in crystalline ice (Schmitt et al., 1998; Brown et al., 2006; Newman et al., 2008). Note that the 1.65 µm absorption band is also sensitive to the water ice temperature, being deeper for colder temperatures of crystalline ice (Grundy and Schmitt, 1998; Grundy et al., 1999).

In our study, we have focused our efforts on eight wavelengths (Fig. 3), including absorption bands at 1.5, 1.65 and 2.0 µm and the reflectance peak at 3.6 µm. We have chosen not to use the Fresnel reflection peak to derive our photometric function, as data are often too noisy around this wavelength and are thus not suitable for our study. The other selected wavelengths (*i.e.,* 1.35, 1.8, 2.25 and 2.55 µm) are intentionally located outside characteristic

water ice absorption bands. At wavelengths longer than 3 µm, the reflectance is in general noisier than at shorter wavelengths due to intrinsic low reflectance of the surface and a lower instrumental sensitivity. Therefore, we did not use wavelengths larger than 3.6 µm.

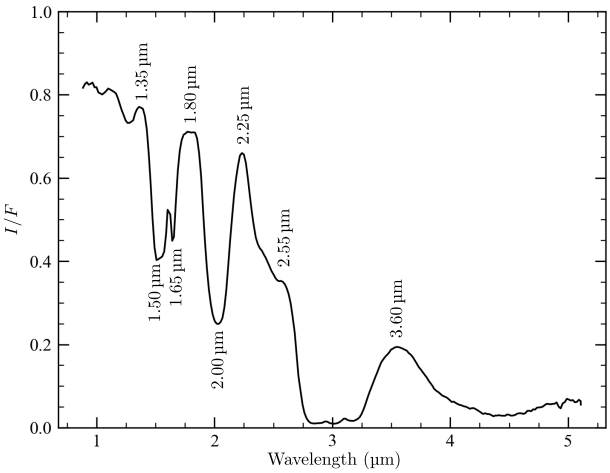


Fig. 3. *Typical I/F spectrum of Enceladus surface, exhibiting the characteristic absorption bands of water ice. Parameters of observation: $i = 39°$, $e = 50°$ and $\alpha = 15°$.*

In order to keep a good signal to noise ratio, we filtered Enceladus' data by selecting pixels having $I/F \leq 0.01$ for each selected wavelength. We have also applied thresholds for each pixel on the values of local angles of incidence and emergence and spatial resolution (see section 2.1). Pixels occurring at the limb and intersecting only part of the surface have been removed.

As a result of this filtering, we first correct data for the disk function (Eq. (4)). We then plot the dependence of the equigonal albedo with the phase (Fig. 4).

We notice variability along the vertical axis. It partly reflects a diverse variety of terrains, associated with different shadowing effects. The significant scatter around 30° of phase corresponds to cubes with a kilometric resolution, which therefore contains a contribution of spatially resolved shadows. This variability is also partly related to pixels occurring near the limb and/or terminator. We did not filter these observations as, despite their extreme observing geometries, they allow an improvement of the spatial coverage and are among the data with the best spatial resolution.

We then apply a linear fit (Eq. (8)) to the data corrected for the disk function (Eq. (4)), thus obtaining parameters a and b, listed in Table 1. The diversity of the values illustrates the spectral dependence of the surface behavior.

3.2.1. Generalizing the phase function

Our objective is to retrieve parameters for any wavelength, including those often affected by a low signal to noise ratio, such as around the Fresnel peak (3.1 µm), which is characteristic of the crystallinity of the ice (see section 3.2). Once the parameters a and b are computed

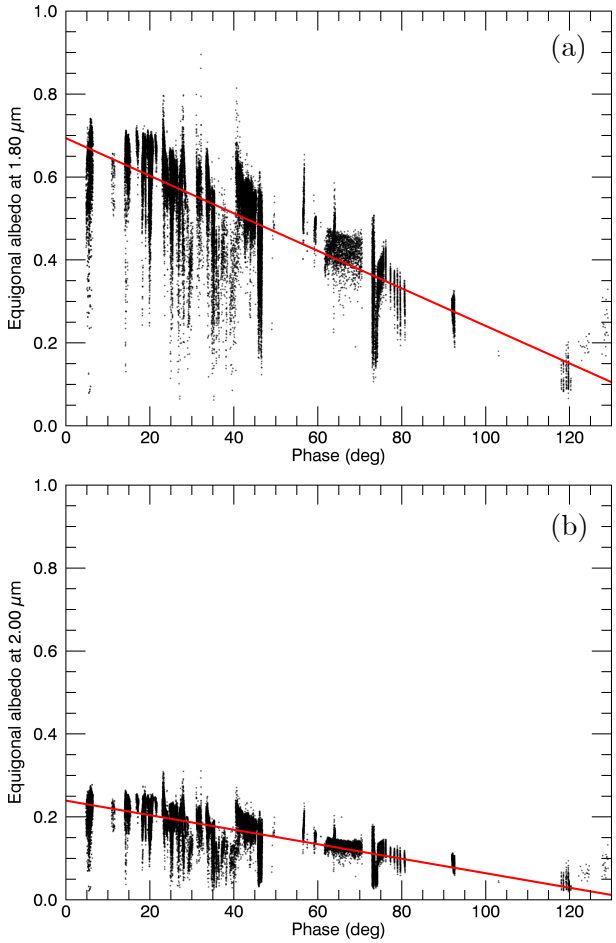


Fig. 4. *Enceladus' phase curves at 1.8 µm (a) and 2.0 µm (b). The red curves correspond to the fit computed on the entire dataset for $(i, e) < 80°$ and $\alpha < 130°$.*

Tab. 1. *Photometric fit parameters, valid for $(i, e) < 80°$ and $\alpha < 130°$.*

Wavelength (µm)	a	b (rad^{-1})
1.3595	0.771	-0.268
1.5079	0.394	-0.156
1.6567	0.483	-0.193
1.8040	0.698	-0.250
2.0017	0.242	-0.098
2.2495	0.638	-0.226
2.5644	0.333	-0.121
3.5961	0.186	-0.085

at the eight selected key wavelengths, we notice that they strongly correlate: the ratio b/a is nearly constant (Fig. 5).

The final photometric model we have derived in this work is the following:

$$I/F = \cos\left(\frac{\alpha}{2}\right) \cdot \cos\left[\frac{\pi}{\pi - \alpha}\left(\gamma - \frac{\alpha}{2}\right)\right] \cdot \frac{(\cos\beta)^{\frac{\alpha}{\pi-\alpha}}}{\cos\gamma} \cdot a \cdot (1 - 0.37\alpha) \quad (9)$$

Where α is the phase angle, γ the photometric longitude, β the photometric latitude and a the zero phase angle

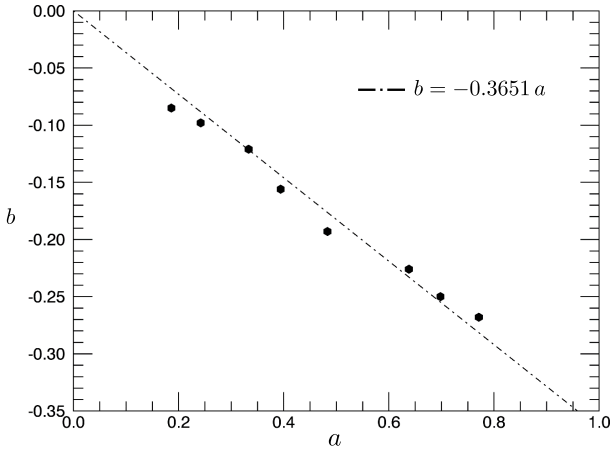


Fig. 5. *Correlation between phase function parameters a and b.*

equigonal albedo. The photometric latitude and longitude are related to the local angles of incidence and emergence (see Eq. (5) and Eq. (7)). The angles are expressed in radians. It should be noted that the model only depends on the illumination and viewing conditions and the wavelength.

3.3. Application of the new photometric function to global mosaics

In this section, we focus on one of our selected wavelengths (1.8 µm), located outside absorption bands characteristic of water ice. Fig. 6 shows the correlation between the reflectance at 1.8 µm and the photometric function we have derived (Eq. (9)). The linear behavior confirms that the photometric function corrects at first order for the incidence, emergence and phase variations. Data out of the main trend, representing less than 3 % of the total data, correspond mostly to pixels with resolved shadows, or located along the Tiger Stripes or occurring near the limb and/or terminator.

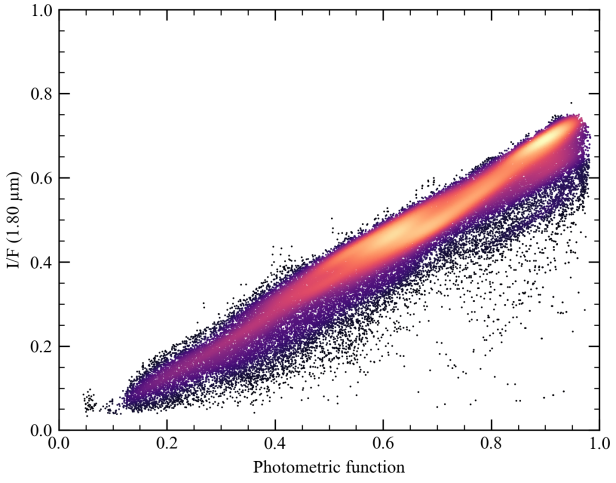


Fig. 6. *I/F at 1.8 µm versus the derived photometric function (see Eq. (9)).*

The global map at 1.8 µm corrected for the photometry with the function described in Eq. (9) is shown in Fig. 7. This photometric correction allows a significant reduction of the level of seams in almost all regions. The remaining ones seem to be related to pixels occurring having extreme observing conditions. Other global maps, derived from various other photometric tests, are provided in the supplementary material (Fig. A.1 and Fig. A.2). The association of the Akimov disk function with a linear phase function was the best trade-off we were able to obtain.

As we have computed the phase function parameters at 8 wavelengths and used an interpolation to extrapolate the correction to the 256 spectral channels, we can obtain corrected reflectance spectra. To better illustrate the effect of the photometric correction, we compare spectra of two points close to each other located in a region with a significant seam on the mosaic (blue and red crosses on Fig. 8a) before photometric correction. The first is located at 22.5°N, 85°E while the second is located at 23.5°N, 88°E. The geometry of observation and illumination is very different from a point to another. Fig. 8 compares these spectra before (Fig. 8a) and after (Fig. 8b) the photometric correction. Spectra are similar after the photometric correction, revealing a homogenous terrain which is confirmed by the ISS map. The photometric correction thus allows to compare spectra independently of illumination and observation conditions.

Fig. 9 shows a comparison of the map before and after the photometric correction in orthographic projection centered on the North Pole and the South Pole. We can see that the application of the new photometric correction reveals features and particularly emphasizes brightness variations across the Tiger Stripes.

4. Spectral diversity

To investigate the spectral diversity of Enceladus' surface, we have computed RGB false color composites of photometrically corrected mosaics, assuming a specific set of color channel attributions. The red, green and blue channels correspond respectively to the ratio between 3.1 and 1.65 µm bands, 2.0 µm and 1.8 µm. These wavelengths have been selected to emphasize variations of the ice physical state. We deliberately use a mix of a ratio (red) and single bands (green and blue) to keep the dependence with the albedo patterns while still emphasizing color variations. As aforementioned, both 3.1 and 1.65 µm bands are indicators of the ice crystallinity (see section 3.2). The ratio between the two bands thus enhances the variations due to ice crystallinity, as 3.1 µm is the Fresnel reflection peak while the 1.65 µm is an absorption band. The 2.0 µm channel represents the center of a strong water ice absorption band, while the 1.8 µm channel falls in the continuum outside of water ice bands. For the composites, we have computed a median of 3 spectral channels (*i.e.,* 134, 135 and 136 at 3.08 µm, 3.10 µm and 3.11 µm) for the Fresnel peak to be less dependent on noise.

Consistent with the results of Brown et al. (2006), we observe a strong enhancement of the red color along the

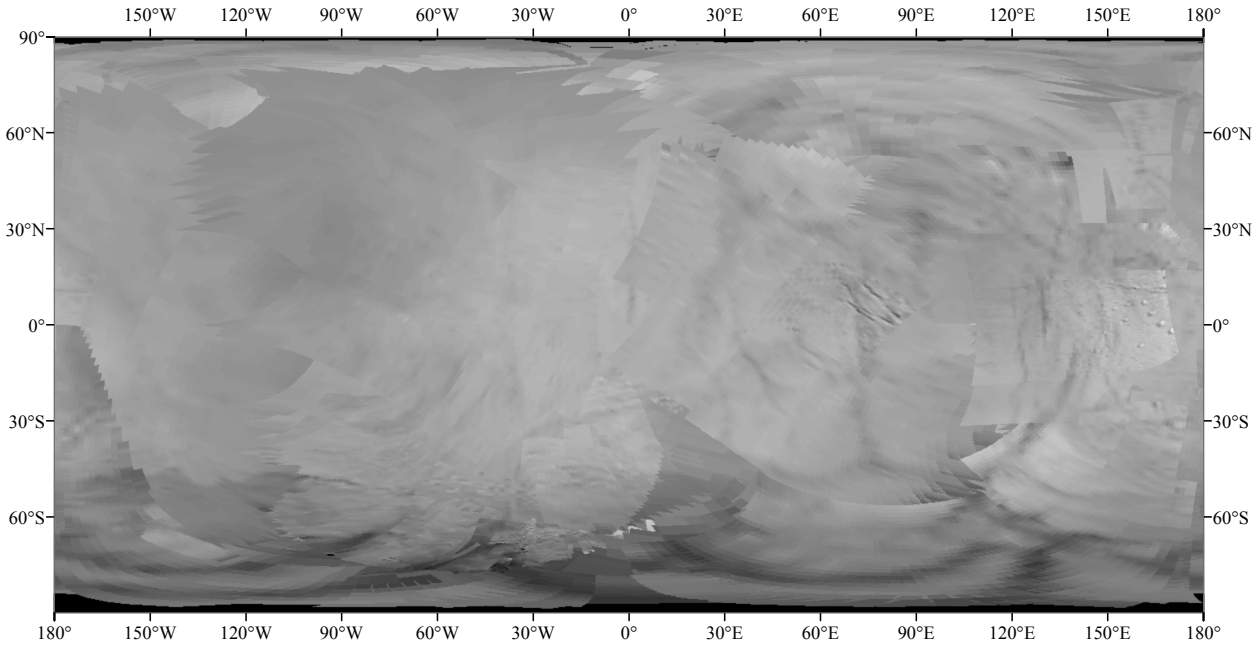


Fig. 7. *Equigonal albedo map at 1.8 µm normalized to unity at zero phase angle.*

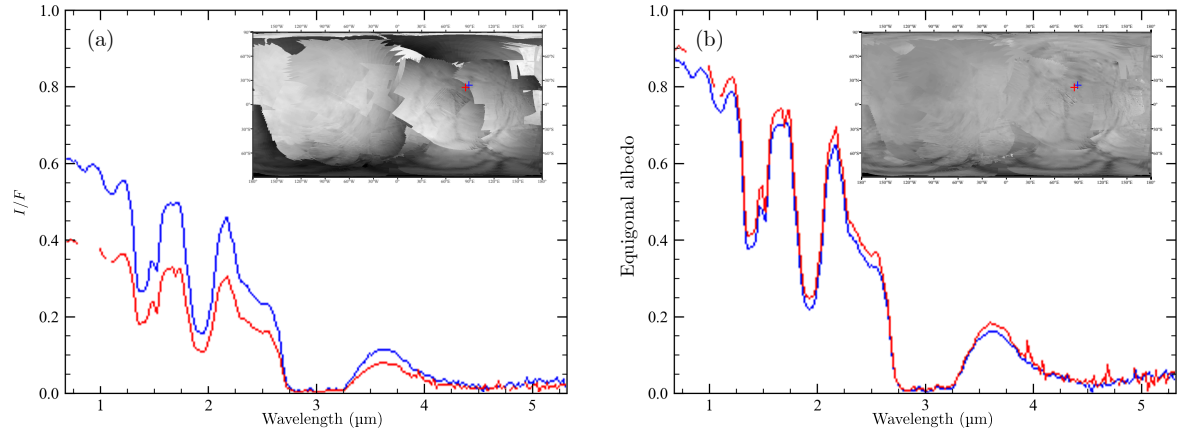


Fig. 8. *Spectrum comparison before (a) and after (b) the photometric correction. The red spectrum corresponds to the cube 1487299582_1 located at 22.5° N, 85° E (i = 72°, e = 49°, α = 26°) while the blue spectrum corresponds to the cube 1489049741_1 located at 23.5° N, 88° E (i = 50°, e = 65°, α = 45°).*

Tiger Stripes (Fig. 11b), revealing the highest degree of crystallinity (highest 3.1 µm peak and most pronounced 1.65 µm absorption band, resulting in the highest 3.1/1.65 ratio, see Fig. 10 and Fig. 11). Interestingly, this RGB color composite reveals a clear boundary in the circumpolar terrain between the leading hemisphere and southern curvilinear terrains as defined by Crow-Willard and Pappalardo (2015) (white arrows on Fig. 11a and Fig. 11c). This suggests that spectral variations in these areas are primarily controlled by geological processes and not mainly driven by particle deposits as proposed by previous studies (Schenk et al., 2011; Scipioni et al., 2017).

Note that residual bright red dots cannot be unambiguously related to any particular spectral feature. They likely correspond to noise, all the more so as they do not really show up in the cube displayed on Fig. 12, which is acquired with a long-time exposure (therefore with a better signal to noise ratio). As already mentioned in section 3.2, the wavelengths longer than 3 µm are generally more affected by the noise.

The RGB composite shown in Fig. 10 contains a red area centered around 30°N, 90°W which was previously identified by different studies (Ries and Janssen, 2015; Scipioni et al., 2017; Combe et al., 2019). As the global map in Fig. 10 still shows some residual seams, we decided to use a single cube in this specific map of Fig. 12 in order to minimize the photometric effects and to also check the consistency of the spectral signature. We show that this area is well correlated with the Leading Hemisphere smooth unit defined by Crow-Willard and Pappalardo (2015). Notably, the southern boundary of this unit coincides relatively well with the limit of the reddish area. We also notice a few reddish zones between 15° and 30°S which appear correlated with major trough features.

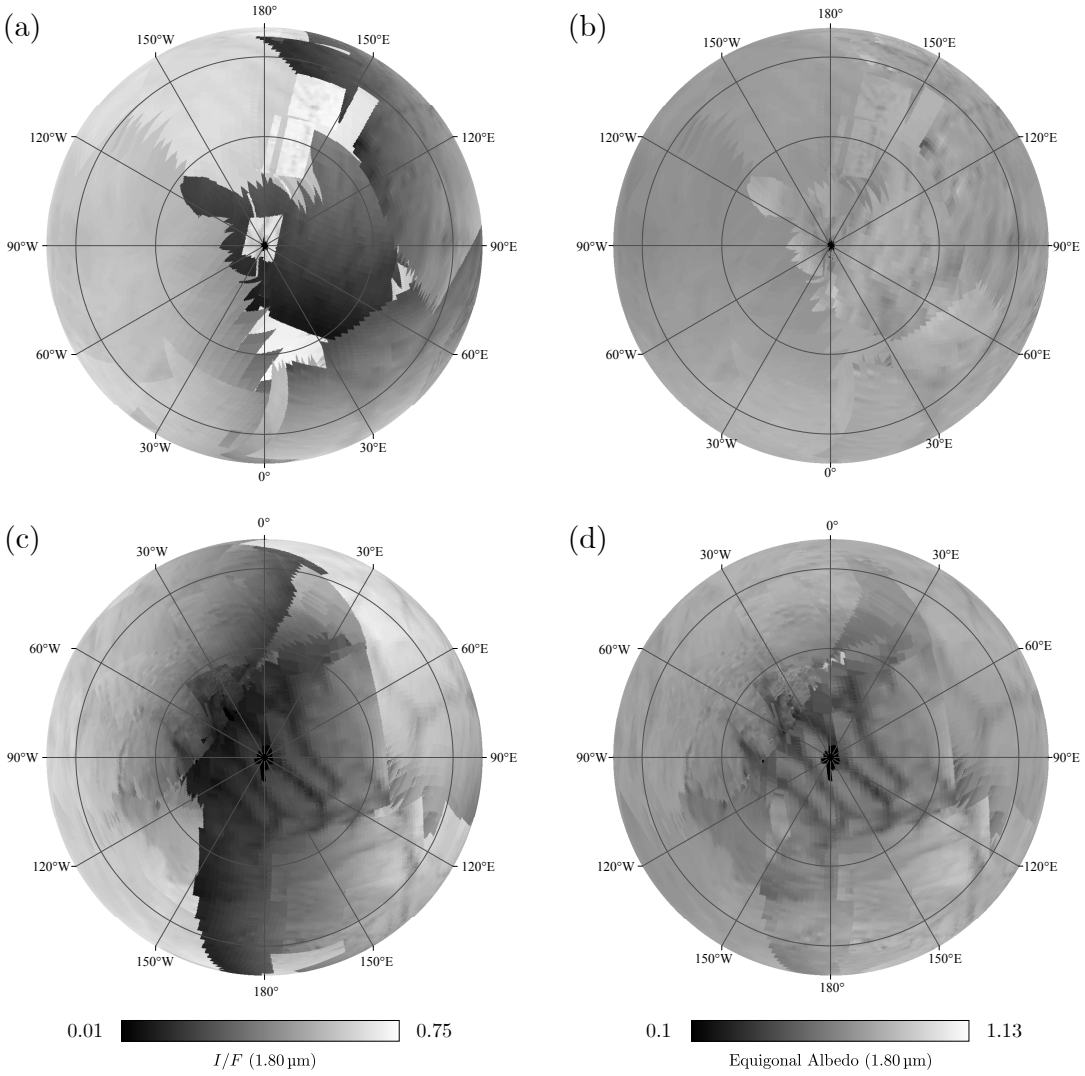


Fig. 9. *Uncorrected mosaic at 1.8 µm in orthographic projection centered on the North Pole (a) and the South Pole (c). 1.8 µm map corrected with the photometric function described in Eq. (9) centered on the North Pole (b) and the South Pole (d).*

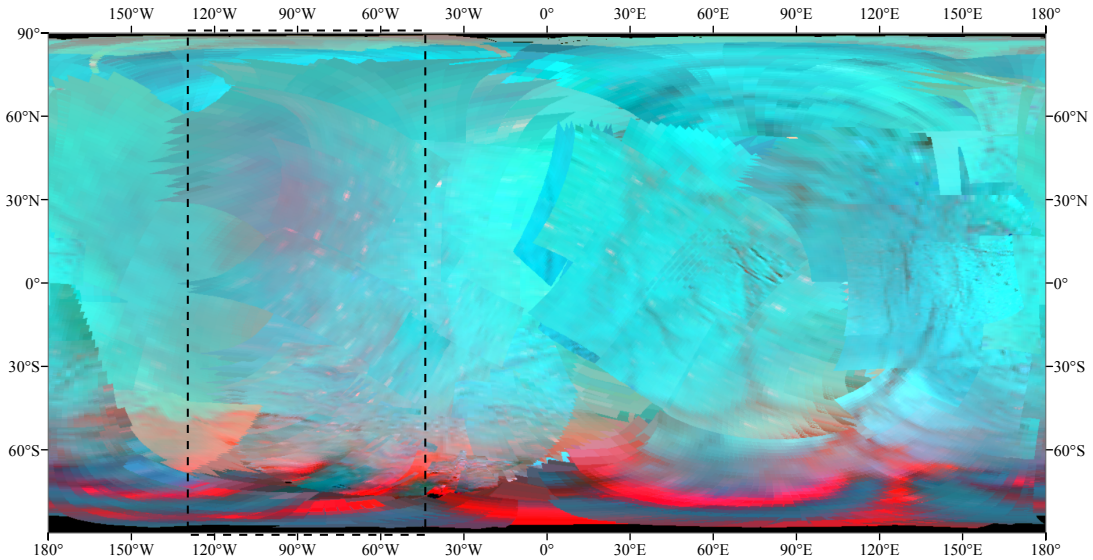


Fig. 10. *RGB global map in equirectangular projection with the red, green and blue channels controlled by the 3.1/1.65 µm ratio, 2.0 µm and 1.8 µm channels respectively. The black dashed line rectangle corresponds to an area discussed in Fig. 12.*

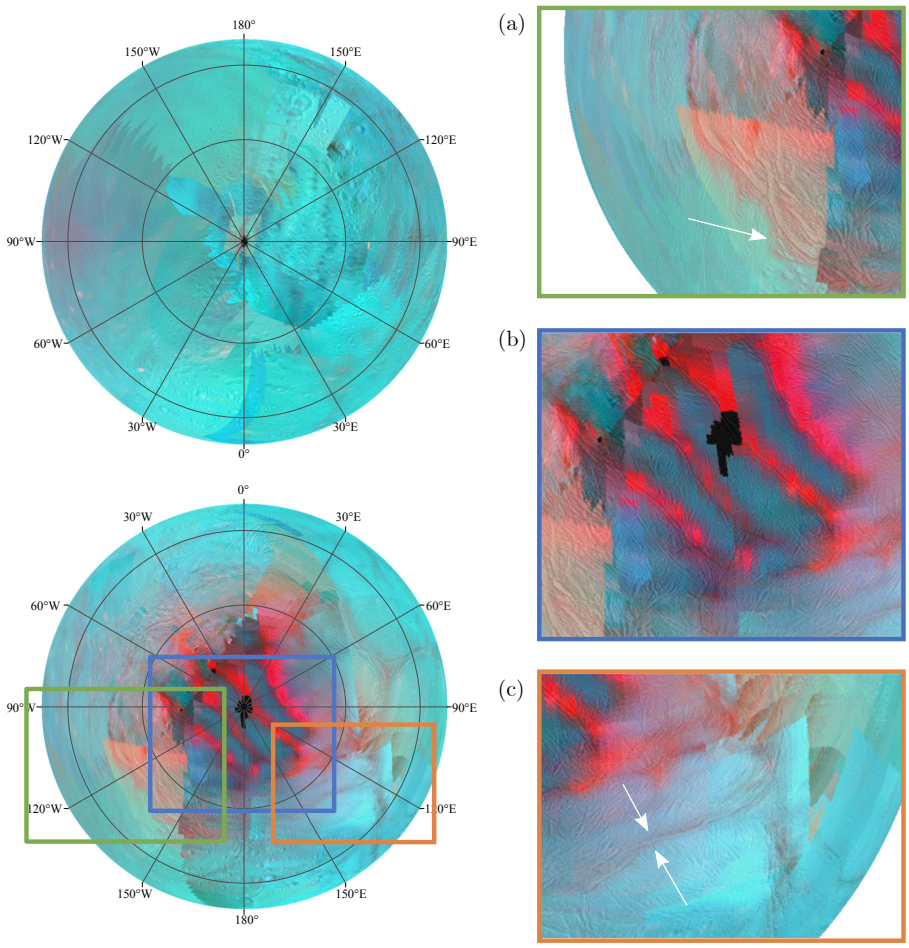


Fig. 11. *Orthographic views derived from the RGB corrected color map (Fig. 10) overlapped on ISS mosaic produced by Bland et al. (2018). The top left image is centered at Enceladus' North Pole whereas the bottom left one is centered at Enceladus' South Pole. Images (a), (b) and (c) show zooms of Enceladus' South Pole.*

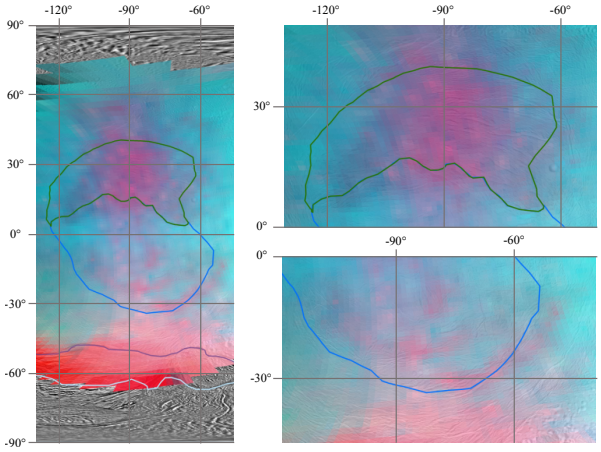


Fig. 12. *Correlation between our VIMS RGB composite representation, corresponding to the black rectangle on Fig. 10 and the geological units as defined by Crow-Willard and Pappalardo (2015). The green line delimits the Leading Hemisphere smooth unit, the blue one delimits the central Leading Hemisphere terrain, the purple one delimits the southern curvilinear unit whereas the cyan one delimits the central south polar unit. The RGB composite was applied on one specific cube (cube: 1702359174_1). We have superimposed the result on ISS mosaic by Bland et al. (2018).*

The corrected spectral map indicates that the main spectral variations are well correlated with several tectonized terrains, suggesting that these variations are mostly controlled by endogenous processes. The reddish zones are indicative of enhanced ice crystallinity, implying that fresh water ices have been exposed geologically recently. It is difficult to really constrain the age of the different reddish terrains, but we can at least conclude that, outside the south polar terrain, the Leading Hemisphere smooth unit centered at 30°N and 90°W is the youngest terrain. Its longitudinal location is consistent with the predictions of Choblet et al. (2017) concerning preferential seafloor hotspot locations along the 90° meridian. Compared to seafloor hotspots located in polar regions, Choblet et al. (2017) predicted that hotspots occurring at mid-latitude along this meridian are more chaotic in nature, and do not remain stable more than a few million years. The reddish spectral behavior of this area indicates that it has likely been active in a recent past, potentially during a period of higher orbital eccentricity and enhanced tidal dissipation in the porous rock core of Enceladus.

5. Conclusion

We have processed the entire VIMS hyperspectral archive of Enceladus in order to compute a global mosaic. The selection of data was based on automatic filters and manual refinement using the previews provided on the website vims.univ-nantes.fr. 355 cubes were merged to produce a global map at 16 pixels per degree.

The product of this refined dataset required the correction of illumination effects. The disk function is based on the Akimov model. We have derived a new empirical phase function. This new photometric function allows to decrease the level of seams in the mosaics of Enceladus computed from the global VIMS data archive. Some seams are, however, still present. They are mostly due to data acquired in strongly varying observing conditions and thus difficult to reconcile with each other into homogeneous mosaics. Some data having extreme observing conditions (*e.g.,* near the limb and/or terminator) were not filtered out as they improve the spatial coverage and provide the best spatial resolution. The study was a true compromise between the quality of the mosaic and the spatial coverage. For future studies, these data could be filtered out in order to improve the derivation of the photometric function. Nonetheless, it will be challenging to completely erase the seams due to strong variability in spatial resolution, pointing conditions and observing geometry. An orbiter around Enceladus would provide a much more optimized cartographic data set compared to the series of distant flybys performed by Cassini.

Furthermore, we produced a new global color map which strongly emphasizes the distribution of the main spectral units, particularly near the Tiger Stripes. The area centered around 30°N, 90°W is correlated with the Leading Hemisphere smooth terrain defined by Crow-Willard and Pappalardo (2015), and may be the signature of recent activity driven by seafloor hotspots, comparable to the south polar activity (Choblet et al., 2017). We plan in further studies to apply this new photometric function to other icy satellites, to evaluate possible differences with Enceladus.

Acknowledgements

This work acknowledges the financial support from CNES, based on observations with Cassini/VIMS, as well as in preparation of the ESA JUICE mission, and from Région Pays de la Loire, project GeoPlaNet (convention #2016-10982). The authors thank R. Pappalardo and A. Patthoff for kindly providing us their structural-geological map of Enceladus. Authors are very grateful to G. Filacchione and S. Schröder for their detailed and helpful comments.

References

Acton C. H. Ancillary data services of NASA's navigation and Ancillary Information Facility. *Planetary and Space Science*, 4465–70, **1996**.

Akimov L. A. Influence of mesorelief on the brightness distribution over a planetary disk. *Soviet Astronomy*, 19385–388, **1976**.

Akimov L. A. Light reflection by the moon. *Kinematika i Fizika Nebesnykh Tel*, 43–10, **1988**.

Bland M. T. and 10 colleagues. A New Enceladus Global Control Network, Image Mosaic, and Updated Pointing Kernels From Cassini's 13-Year Mission. *Earth and Space Science*, 5(10)604–621, **2018**.

Brown R. H. and 21 colleagues. The Cassini Visual and Infrared Mapping Spectrometer (VIMS) Investigation. In *The Cassini-Huygens Mission*, pp 111–168. Kluwer Academic Publishers, **2004**.

Brown R. H. and 24 colleagues. Composition and Physical Properties of Enceladus' Surface. *Science*, 311(5766)1425–1428, **2006**.

Buratti B. and Veverka J. Voyager photometry of Rhea, Dione, Tethys, Enceladus and Mimas. *Icarus*, 58(2)254–264, **1984**.

Buratti B. J. Voyager disk resolved photometry of the Saturnian satellites. *Icarus*, 59(3)392–405, **1984**.

Buratti B. J. and Veverka J. Photometry of rough planetary surfaces: The role of multiple scattering. *Icarus*, 64(2)320–328, **1985**.

Choblet G. and 6 colleagues. Powering prolonged hydrothermal activity inside Enceladus. *Nature Astronomy*, 1(12)841–847, **2017**.

Clark R. N. and Lucey P. G. Spectral properties of ice-particulate mixtures and implications for remote sensing: 1. Intimate mixtures. *Journal of Geophysical Research: Solid Earth*, 89(B7)6341–6348, **1984**.

Clark R. N. and 3 colleagues. Observed Ices in the Solar System. In *The Science of Solar System Ices*, pp 3–46. Springer, **2013**.

Clark R. N. and 3 colleagues. The VIMS Wavelength and Radiometric Calibration 19, Final Report. The Planetary Atmospheres Node, **2018**.

Combe J.-P. and 6 colleagues. Reflectance properties and hydrated material distribution on Vesta: Global investigation of variations and their relationship using improved calibration of Dawn VIR mapping spectrometer. *Icarus*, 25921–38, **2015**.

Combe J.-P. and 6 colleagues. Nature, distribution and origin of CO2 on Enceladus. *Icarus*, 317491–508, **2019**.

Crow-Willard E. N. and Pappalardo R. T. Structural mapping of Enceladus and implications for formation of tectonized regions. *Journal of Geophysical Research: Planets*, 120(5)928–950, **2015**.

Cruikshank D. P. and 9 colleagues. A spectroscopic study of the surfaces of Saturn's large satellites: H2O ice, tholins, and minor constituents. *Icarus*, 175(1)268–283, **2005**.

Dalton J. B. and 6 colleagues. Chemical Composition of Icy Satellite Surfaces. *Space Science Reviews*, 153(1)113–154, **2010**.

Domingue D. L. and 3 colleagues. Application of multiple photometric models to disk-resolved measurements of Mercury's surface: Insights into Mercury's regolith characteristics. *Icarus*, 268172–203, **2016**.

Dougherty M. K. and 6 colleagues. Identification of a Dynamic Atmosphere at Enceladus with the Cassini Magnetometer. *Science*, 311(5766)1406–1409, **2006**.

Filacchione G. and 18 colleagues. Saturn's icy satellites and rings investigated by Cassini–VIMS: III – Radial compositional variability. *Icarus*, 220(2)1064–1096, **2012**.

Filacchione G. and 8 colleagues. Photometric Modeling and VIS-IR Albedo Maps of Tethys From Cassini-VIMS. *Geophysical Research Letters*, 45(13)6400–6407, **2018a**.

Filacchione G. and 8 colleagues. Photometric Modeling and VIS-IR Albedo Maps of Dione From Cassini-VIMS. *Geophysical Research Letters*, 45(5)2184–2192, **2018b**.

Filacchione G. and 15 colleagues. Saturn's icy satellites investigated by Cassini-VIMS. IV. Daytime temperature maps. *Icarus*, 271 292–313, **2016**.

Fink U. and Larson H. P. Temperature dependence of the water-ice spectrum between 1 and 4 microns: Application to Europa, Ganymede and Saturn's rings. *Icarus*, 24(4)411–420, **1975**.

Grundy W. M. and Schmitt B. The temperature-dependent near-infrared absorption spectrum of hexagonal H2O ice. *Journal of Geophysical Research: Planets*, 103(E11)25809–25822, **1998**.

Grundy W. M. and 4 colleagues. Near-Infrared Spectra of Icy Outer Solar System Surfaces: Remote Determination of H2O Ice Temperatures. *Icarus*, 142(2)536–549, **1999**.

Hansen C. J. and 7 colleagues. Enceladus' Water Vapor Plume. *Science*, 311(5766)1422–1425, **2006**.

Hansen G. B. and McCord T. B. Amorphous and crystalline ice on the Galilean satellites: A balance between thermal and radiolytic processes. *Journal of Geophysical Research: Planets*, 109(E1), **2004**.

Hapke B. Bidirectional reflectance spectroscopy: 1. Theory. *Journal of Geophysical Research: Solid Earth*, 86(B4)3039–3054, **1981**.

Hapke B. *Theory of Reflectance and Emittance Spectroscopy*. Cambridge University Press, second edition, **2012**.

Hapke B. W. A theoretical photometric function for the lunar surface. *Journal of Geophysical Research*, 68(15)4571–4586, **1963**.

Jaumann R. and 18 colleagues. Distribution of icy particles across Enceladus' surface as derived from Cassini-VIMS measurements. *Icarus*, 193(2)407–419, **2008**.

Kreslavsky M. A. and 5 colleagues. Photometric properties of the lunar surface derived from Clementine observations. *Journal of Geophysical Research: Planets*, 105(E8)20281–20295, **2000**.

Le Mouélic S. and 13 colleagues. The Cassini VIMS archive of Titan: From browse products to global infrared color maps. *Icarus*, 319 121–132, **2019**.

Minnaert M. The reciprocity principle in lunar photometry. *The Astrophysical Journal*, 93403–410, **1941**.

Newman S. F. and 5 colleagues. Photometric and spectral analysis of the distribution of crystalline and amorphous ices on Enceladus as seen by Cassini. *Icarus*, 193(2)397–406, **2008**.

Nicholson P. D. and 11 colleagues. Occultation observations of Saturn's rings with Cassini VIMS. *Icarus*, **2019**.

Oancea A. and 6 colleagues. Laboratory infrared reflection spectrum of carbon dioxide clathrate hydrates for astrophysical remote sensing applications. *Icarus*, 221(2)900–910, **2012**.

Porco C. C. and 24 colleagues. Cassini Observes the Active South Pole of Enceladus. *Science*, 311(5766)1393–1401, **2006**.

Ries P. A. and Janssen M. A large-scale anomaly in Enceladus' microwave emission. *Icarus*, 25788–102, **2015**.

Schenk P. and 6 colleagues. Plasma, plumes and rings: Saturn system dynamics as recorded in global color patterns on its midsize icy satellites. *Icarus*, 211(1)740–757, **2011**.

Schmitt B. and 3 colleagues. Optical Properties of Ices From UV to Infrared. In *Solar System Ices*, pp 199–240. Springer Netherlands, **1998**.

Schröder S. E. and 4 colleagues. Resolved photometry of Vesta reveals physical properties of crater regolith. *Planetary and Space Science*, 85198–213, **2013**.

Schröder S. E. and 11 colleagues. Resolved spectrophotometric properties of the Ceres surface from Dawn Framing Camera images. *Icarus*, 288201–225, **2017**.

Scipioni F. and 6 colleagues. Deciphering sub-micron ice particles on Enceladus surface. *Icarus*, 290183–200, **2017**.

Shkuratov Y. and 5 colleagues. Optical measurements of the Moon as a tool to study its surface. *Planetary and Space Science*, 59 (13)1326–1371, **2011**.

Shkuratov Y. G. and 6 colleagues. Opposition Effect from Clementine Data and Mechanisms of Backscatter. *Icarus*, 141(1)132–155, **1999**.

Smith B. A. and 28 colleagues. A New Look at the Saturn System: The Voyager 2 Images. *Science*, 215(4532)504–537, **1982**.

Spahn F. and 15 colleagues. Cassini Dust Measurements at Enceladus and Implications for the Origin of the E Ring. *Science*, 311 (5766)1416–1418, **2006**.

Spencer J. R. and 9 colleagues. Cassini Encounters Enceladus: Background and the Discovery of a South Polar Hot Spot. *Science*, 311 (5766)1401–1405, **2006**.

Squyres S. W. and 3 colleagues. The evolution of Enceladus. *Icarus*, 53(2)319–331, **1983**.

Taffin C. and 5 colleagues. Temperature and grain size dependence of near-IR spectral signature of crystalline water ice: From lab experiments to Enceladus' south pole. *Planetary and Space Science*, 61(1)124–134, **2012**.

Verbiscer A. J. and Veverka J. A Photometric Study of Enceladus. *Icarus*, 110(1)155–164, **1994**.

Waite J. H. and 13 colleagues. Cassini Ion and Neutral Mass Spectrometer: Enceladus Plume Composition and Structure. *Science*, 311(5766)1419–1422, **2006**.

Appendix A. Supplementary material

This supplementary material aims to provide the reader with additional information on the different photometric functions that have been tested during the study. We used non-linear least squares to fit the photometric functions to data. The tested functions are summarized in the following table (Table A.2). The standard deviation errors correspond to the square root of the estimated covariance matrix diagonal. The corresponding parameters were computed by minimizing the standard deviation error. The resulting mosaics are presented in Fig. A.1 and Fig. A.2 for one specific wavelength (1.8 µm). The first figure (Fig. A.1) illustrates the difference between two models of disk functions (Akimov and parametrized Akimov). It also highlights the differences regarding the phase function, whether we choose a linear phase function or an exponential one. The complete photometric function is mentioned above the corresponding map. The second figure (Fig. A.2) shows two other disk functions (Lommel-Seeliger/Lambert and Minnaert models) combined with linear and exponential phase functions. Please note that we took the disk function parameter k constant with phase. A possibility for future studies would be to consider k linearly dependent with the phase as proposed by Schröder et al. (2017).

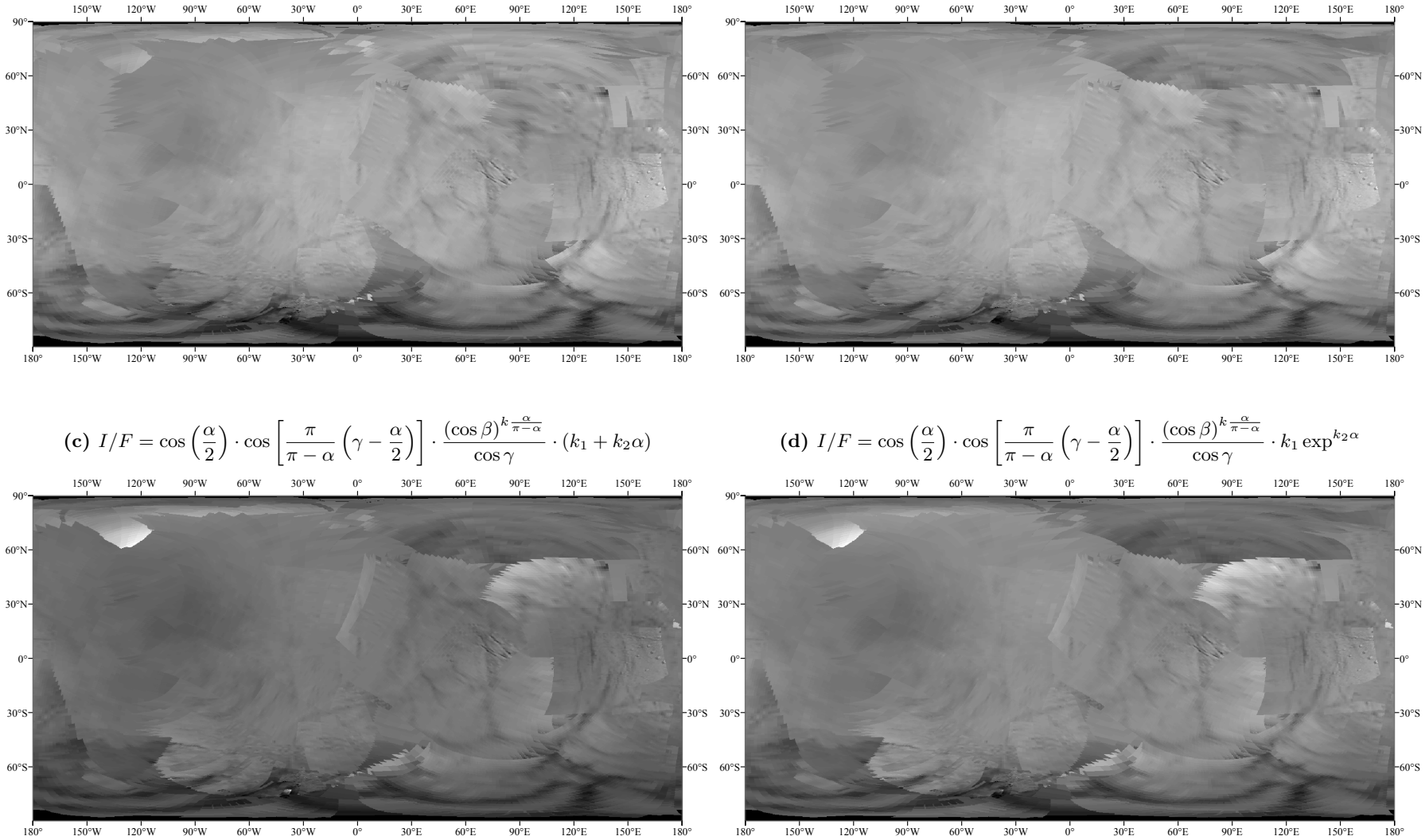
We notice that the association of the parametrized Akimov disk function with a linear phase function provides the best standard deviation errors for the computed parameters. However, the fit improvement remains small. Moreover, the resulting mosaic is downgraded relative to the one corrected for the association of the Akimov disk function with the linear phase function. The exponential phase function does improve the correction on some parts but deteriorates some others.

Tab. A.2. *Coefficients for the disk function and phase function parameters, computed for I/F at 1.8 µm. Parameters are valid for $(i, e) < 80°$ and $\alpha < 130°$. We evaluate the performance of photometric models by calculating the standard deviation errors.*

		Parameters			Standard deviation errors		
Disk function	Phase function	k	k_1	k_2	$\sigma(k)$	$\sigma(k_1)$	$\sigma(k_2)$
Akimov	Linear		0.698	-0.250		$5.7 \cdot 10^{-4}$	$8.5 \cdot 10^{-4}$
	Exponential		0.716	-0.464		$7.5 \cdot 10^{-4}$	$1.8 \cdot 10^{-3}$
Parametrized Akimov	Linear	2.422	0.717	-0.243	$1.3 \cdot 10^{-2}$	$5.5 \cdot 10^{-4}$	$8.0 \cdot 10^{-4}$
	Exponential	2.421	0.731	-0.427	$1.3 \cdot 10^{-2}$	$6.9 \cdot 10^{-4}$	$1.7 \cdot 10^{-3}$
Minnaert	Linear	0.741	0.806	-0.340	$7.7 \cdot 10^{-4}$	$6.8 \cdot 10^{-4}$	$7.9 \cdot 10^{-4}$
	Exponential	0.748	0.860	-0.619	$7.6 \cdot 10^{-4}$	$8.8 \cdot 10^{-4}$	$1.5 \cdot 10^{-3}$
L-S/Lambert	Linear	0.421	0.813	-0.333	$1.6 \cdot 10^{-3}$	$7.0 \cdot 10^{-4}$	$8.2 \cdot 10^{-4}$
	Exponential	0.406	0.863	-0.592	$1.5 \cdot 10^{-3}$	$9.0 \cdot 10^{-4}$	$1.5 \cdot 10^{-3}$

(a) $I/F = \cos\left(\frac{\alpha}{2}\right) \cdot \cos\left[\frac{\pi}{\pi-\alpha}\left(\gamma - \frac{\alpha}{2}\right)\right] \cdot \frac{(\cos\beta)^{\frac{\alpha}{\pi-\alpha}}}{\cos\gamma} \cdot (k_1 + k_2\alpha)$

(b) $I/F = \cos\left(\frac{\alpha}{2}\right) \cdot \cos\left[\frac{\pi}{\pi-\alpha}\left(\gamma - \frac{\alpha}{2}\right)\right] \cdot \frac{(\cos\beta)^{\frac{\alpha}{\pi-\alpha}}}{\cos\gamma} \cdot k_1 \exp^{k_2\alpha}$



(c) $I/F = \cos\left(\frac{\alpha}{2}\right) \cdot \cos\left[\frac{\pi}{\pi-\alpha}\left(\gamma - \frac{\alpha}{2}\right)\right] \cdot \frac{(\cos\beta)^{k\frac{\alpha}{\pi-\alpha}}}{\cos\gamma} \cdot (k_1 + k_2\alpha)$

(d) $I/F = \cos\left(\frac{\alpha}{2}\right) \cdot \cos\left[\frac{\pi}{\pi-\alpha}\left(\gamma - \frac{\alpha}{2}\right)\right] \cdot \frac{(\cos\beta)^{k\frac{\alpha}{\pi-\alpha}}}{\cos\gamma} \cdot k_1 \exp^{k_2\alpha}$

Fig. A.1. *Mosaic at 1.8 μm corrected with (a) Akimov disk function and linear phase function, (b) Akimov disk function and exponential phase function, (c) parametrized Akimov disk function and linear phase function and (d) parametrized Akimov disk function and exponential phase function.*

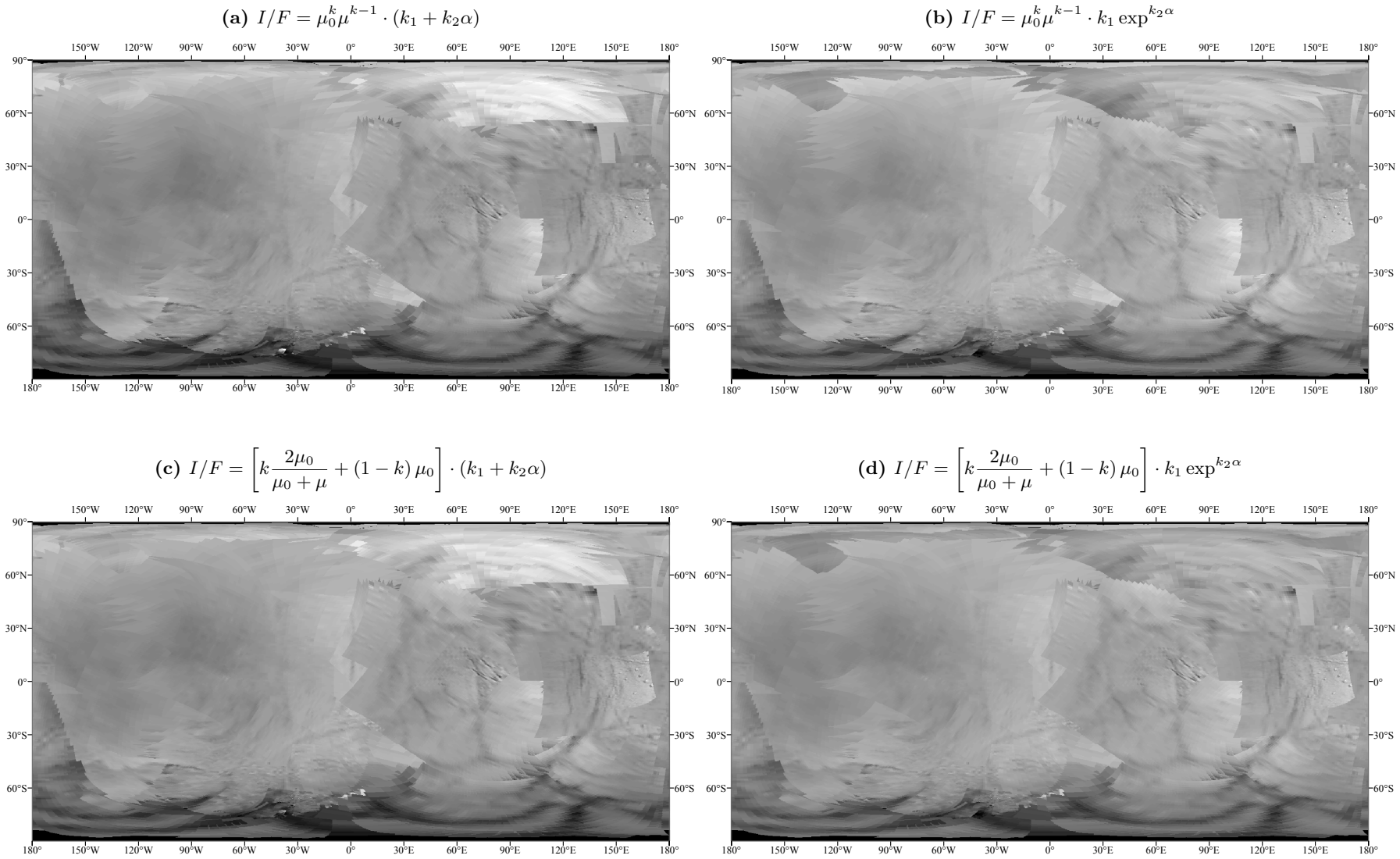


Fig. A.2. *Mosaic at 1.8 μm corrected with (a) Minnaert disk function and linear phase function, (b) Minnaert disk function and exponential phase function, (c) L-S/Lambert disk function and linear phase function and (d) L-S/Lambert disk function and exponential phase.*